Scientific Reports

https://doi.org/10.1038/s41598-026-49356-8

Article in Press

Small disturbance oscillation suppression strategy for doubly-fed wind turbine based on joint control of LADRC and AQPR

Received: 6 June 2025

Accepted: 14 April 2026

Published online: 22 April 2026

Cite this article as: Li C., Liang C., Zhang J. *et al.* Small disturbance oscillation suppression strategy for doubly-fed wind turbine based on joint control of LADRC and AQPR. *Sci Rep* (2026). https://doi.org/10.1038/s41598-026-49356-8

Chenchen Li, Chunhui Liang, Jiale Zhang, Renjie Liu, Chenglong Huang, Songcai Zhang & Shuyu Zhang

Small disturbance oscillation suppression strategy for doubly-fed wind turbine based on joint control of LADRC and AQPR

Chenchen Li [1], Chunhui Liang [1,2,*] , Jiale Zhang [1] , Renjie Liu [1] ,Chenglong Huang [1] ,Songcai Zhang[1] and Shuyu Zhang[1]

[1] School of Electrical and Information Engineering, Changchun Institute of Technology, Changchun 130025, China; lichenchen@stu.ccit.edu.cn (L.C.);lch0218080@ccit.edu.cn(L.C.);zhangjiale@stu.ccit.edu.cn (Z.J.); liurenjie@stu.ccit.edu.cn(L.R.); huangchenglong@stu.ccit.edu.cn(H.C.);17730892970@163.com(Z.S.); ZhangShuyu0705@outlook.com(Z.S.).
[2] National local joint Engineering Research Center for Measurement and Control and Safe Operation Technology of Intelligent Distribution Network, Changchun 130103, China;
* Correspondence: lch0218080@ccit.edu.cn(L.C.)

Abstract: To address the issue that small-signal oscillations on the rotor side of doubly fed wind turbines may propagate through multiple transmission paths and induce subsynchronous oscillations, this paper proposes a small-signal oscillation suppression strategy based on the combined control of linear active disturbance rejection control (LADRC) and adaptive quasi-proportional resonant (AQPR) control. LADRC is employed to replace the conventional PI controller in the inner current loop of the rotor-side converter, where real-time disturbance estimation and compensation effectively block the propagation of small-signal oscillations within the current loop. Meanwhile, by integrating the intrinsic time-scale decomposition (ITD)-based oscillation frequency identification algorithm with a frequency-locking update module, an AQPR suppressor is constructed to achieve frequency-selective suppression of time-varying small-signal oscillations embedded in cross-coupled current signals. Based on this framework, an LADRC–AQPR combined current-loop control system is established, and key parameters are optimally designed to mitigate subsynchronous control interactions. Simulation and experimental results further provide systematic comparisons between LADRC-, QPR-, and ITD-based methods and their conventional counterparts in terms of oscillation identification and suppression performance, demonstrating that the proposed method exhibits superior dynamic response and enhanced robustness. Moreover, comparative validations under three typical operating conditions confirm that the proposed combined control strategy significantly outperforms conventional approaches in suppressing small-signal oscillations and can effectively mitigate time-varying small-signal oscillations in grid-connected doubly fed wind turbine systems.

Keywords: Doubly-fed wind turbine; Rotor side converter; Small interference oscillation; Linear active disturbance rejection controller; Adaptive quasi-proportional resonance suppressor

1. Introduction

In order to realize China ’ s carbon peak and carbon neutrality strategic

objectives, wind energy, as a clean energy source in the power system, has experienced rapid and sustained development. Since most wind power generation bases in China are located in remote areas, fixed or controllable series compensation is often adopted to increase line transmission capacity due to long transmission distances and large-scale power delivery [1]. Sub-synchronous oscillation (SSO) accidents caused by series compensation have occurred repeatedly. For example, in 2009, an SSO accident with an oscillation frequency of approximately 25 Hz occurred in a wind farm in Texas, USA [2,3]; in 2012 and 2016, oscillations occurred in wind farms in Guyuan, Hebei Province, and Tongyu, Jilin Province, respectively, where the wind farms were connected to the grid through series-compensated transmission lines, with oscillation frequencies of 6–8 Hz in 2012 and 5.33 Hz in 2016 [4]. Therefore, it is of great significance to study system-level SSO suppression strategies for doubly fed induction generator (DFIG) wind turbine systems connected to the grid via series-compensated transmission lines.

SSO suppression strategies at this stage are generally categorized into three types. For the first type, the key control parameters of the wind turbine converters are adjusted. Literature [5] concludes, through theoretical derivation and simulation verification, that appropriate parameter selection can effectively reduce the occurrence of SSO. This method is easy to implement; however, modifying the key control parameters of the wind turbine converters may adversely affect their dynamic performance and fault ride-through capability, and therefore it is not an ideal solution.

The second type of method is to employ advanced nonlinear controllers to replace conventional proportional–integral (PI) controllers or to introduce additional damping control. For example, $H\infty$ robust controllers [6], feedback linearization controllers [7], and sliding mode controllers [8,9] have been reported. Although these controllers can achieve better control performance, the oscillation suppression strategies rely on accurate modeling of the doubly fed wind turbine system, resulting in relatively complex control structures, and their stable operation is easily affected by external disturbances. In the doubly fed induction generator (DFIG) system, supplementary sub-synchronous damping control is usually implemented in the rotor-side converter (RSC) or grid-side converter (GSC). According to different input signals, supplementary sub-synchronous damping control is generally divided into three types:

1) The RMS value of the line compensation capacitor voltage is used as the input control signal. For example, in literature [10], the line compensation capacitor voltage RMS (V_C) is employed as the input signal of the supplementary sub-synchronous damping controller (SSDC), and its output is embedded in the grid-side converter (GSC). The results show that using V_C as the control signal has a good suppression effect on SSO.

2) The rotor speed is used as the input control signal. As reported in literature [11,12], the rotor speed is simultaneously embedded into the output voltage control loops of the d-axis and q-axis of the rotor-side converter (RSC), and the controller parameters are optimized using an improved particle swarm

optimization algorithm, thereby achieving effective SSO suppression under various operating conditions.

3) The rotor current is used as the input control signal. In literature [13], the d-axis and q-axis components of the rotor current are adopted as input signals, where i_{dr} and i_{qr} serve as the control inputs. Based on i_{dr} and i_{qr}, a rotor-side SSDC is designed for a system in which SSO actually occurs, and the controller performance is verified using a small-signal impedance model.

Literature [14] compares the control effects of the above three SSDCs and concludes that the third type exhibits better control performance; however, it still suffers from the complexity of parameter optimization. Similar to the third type of SSDC, literature [15–17] proposes an SSO suppression strategy by attaching a sub-synchronous notch filter (SNF) to the rotor-side converter (RSC) of the DFIG, and the optimal attachment position of the SNF is determined using a quantitative method based on numerical comparison, which is easy to implement. This type of scheme has the advantages of simple implementation and straightforward parameter tuning. Its limitation is that it is mainly suitable for SSO suppression within a fixed frequency band and cannot effectively suppress SSO outside this frequency range.

The third type of method utilizes flexible AC transmission system (FACTS) devices to achieve centralized suppression of sub-synchronous control interaction (SSCI). Active disturbance rejection control (ADRC) does not rely on an accurate mathematical model of the system and exhibits strong robustness in nonlinear, strongly coupled, and time-varying systems. In literature [18], an additional ADRC-based damping controller is incorporated into a static synchronous compensator (STATCOM) to address the limitation that filter-based suppression strategies cannot adapt to varying operating conditions, which poses challenges in practical engineering applications. In literature [19,20], linear active disturbance rejection control (LADRC) is further proposed, which reduces the number of control parameters to two without degrading control performance. However, the time-delay factor is usually neglected, resulting in a mismatch between observer inputs on the time axis, thereby reducing tracking accuracy and adversely affecting control reliability.

Although the above methods can suppress small-signal oscillations in DFIG grid-connected systems to a certain extent, existing studies on improving wind turbine control strategies mainly focus on suppressing small-signal oscillations within a specific frequency range [21–23]. In practical engineering applications, the oscillation frequency associated with small-signal oscillations varies in real time due to changes in grid conditions and control strategies. As a result, the following two issues arise: (i) when small-signal oscillations occur, multiple oscillation transmission paths exist in the rotor-side converter (RSC) of the doubly fed wind turbine, and the oscillation frequency varies in real time, which increases the difficulty of suppression using conventional turbine control strategy improvements; (ii) the oscillation frequency of small-signal oscillations in the cross-coupled control signals of the RSC also changes in real time, and when the oscillation frequency

varies, the corresponding oscillation frequency in the rotor-side converter of the doubly fed wind turbine changes accordingly, such that the conventional inner-loop current control strategy of the RSC cannot achieve effective suppression.

In summary, this paper has the following three main contributions:

(1) From a mechanism-oriented perspective, the multi-path propagation characteristics of small-signal oscillations in the rotor-side converter of a doubly fed wind turbine through both the current inner loop and the cross-coupling channels are systematically revealed. Meanwhile, the individual components of the LADRC model are introduced in detail, and the conventional PI controller is replaced by LADRC. Comparative experimental results demonstrate that the proposed LADRC-based current inner-loop control can effectively block the propagation paths of small-signal oscillation frequencies in the rotor-side converter.

(2) Based on the mathematical model of the rotor-side controller of the doubly fed wind turbine, an adaptive quasi-proportional resonant (AQPR) suppressor is constructed by integrating the intrinsic time-scale decomposition (ITD) algorithm for oscillation frequency identification with a frequency-locked update module. The proposed AQPR suppressor replaces the conventional SSDC controller, and its key parameters are optimized to achieve effective tracking and suppression of small-signal oscillation frequencies in the current inner-loop control signals of the rotor-side converter.

(3) By combining LADRC and AQPR, a novel integrated control scheme is developed. On a simulation platform of a doubly fed wind turbine grid-connected system with series-compensated transmission lines, simulation results verify that the proposed integrated control strategy outperforms the traditional PI-, PI+SSDC-, and single-controller schemes in terms of oscillation suppression effectiveness, dynamic performance, and robustness.

The rest of this paper is organized as follows:

Section 2 explains the mechanism of small-signal oscillations based on the construction of a grid-connected doubly fed wind turbine system model. Section 3 constructs a joint controller based on the ITD algorithm combined with AQPR and LADRC, and describes the operating principles of the controllers. Section 4 constructs the overall control structure diagram of the joint controller and calibrates the key parameters. Section 5 builds a simulation model of a grid-connected doubly fed wind turbine connected to a series-compensated transmission line on the MATLAB/Simulink platform and analyzes the operational performance of the LADRC suppressor, the AQPR suppressor, and the joint suppressor, respectively. Section 6 summarizes the whole paper.

2. Modelling of doubly-fed wind turbine grid-connected system with explanation of small disturbance oscillation mechanism

2.1. Modeling of grid-connected doubly-fed fan system

The overall model of the doubly fed wind farm connected to a transmission-line-based grid is shown in Figure 1. The doubly fed wind farm consists of 66 individual doubly fed wind turbines with a rated capacity of 1.5 MW each. In the

traditional control of doubly fed wind turbines, the rotor-side converter (RSC) employs decoupled active and reactive power control to achieve maximum power point tracking (MPPT), while the grid-side converter (GSC) adopts fixed DC-link voltage control and reactive power factor control to stabilize the grid-connected AC voltage. A phase-locked loop (PLL) is used to maintain synchronous operation between the wind turbine system and the power grid. The physical meanings of the variables shown in the figure are listed in Table 1 in Section 5.

In Figure 1, the series compensation degree K_C of the transmission line is defined as:

$$K_C = \frac{X_C}{\sum (X_T + X_L)} \quad (1)$$

Where X_C and X_L are the equivalent capacitive reactance and inductive reactance of the series-compensated transmission line, respectively, and X_T is the equivalent inductive reactance of the transformer.

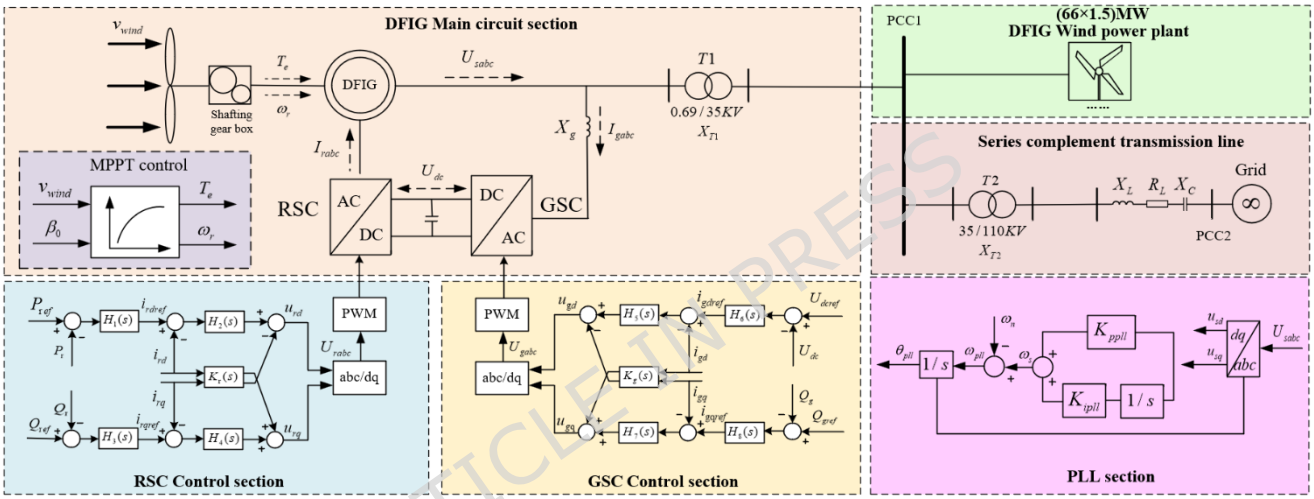

Figure 1. Structure diagram of doubly-fed wind farm system with series-complement transmission lines connected to the grid

Literature [24] points out that variations in wind turbine control components and transmission line parameters can induce small-signal oscillations in the overall grid-connected wind farm system, while representing the entire wind farm as an equivalent single wind turbine remains analytically valid. Therefore, it is assumed that the operating points of all wind turbines in the wind farm are essentially identical at the same time, and the parameters of a single equivalent wind turbine are obtained from the aggregated parameters of the wind farm. Based on capacity weighting, the wind farm can be equivalently represented by a single doubly fed wind turbine model, which is connected to a transmission line containing series compensation capacitors through two-stage step-up transformers T_1 and T_2. Accordingly, this paper employs a single doubly fed wind turbine to represent the entire wind farm for comprehensive analysis.

2.2. Mathematical model of doubly fed induction generator

Under ideal conditions, such as neglecting magnetic saturation and leakage effects, the air-gap magnetic field is assumed to be sinusoidally distributed, and

the windings of the doubly fed induction generator can be equivalently represented by the physical model shown in Figure 2.

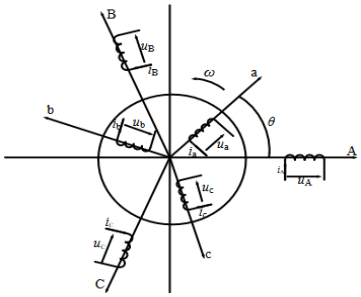

Figure 2. The equivalent physical model of doubly-fed induction generator

The Park transformation is used to convert the three-phase stationary model of a doubly fed induction generator into a two-phase *dq* rotating coordinate system, and the resulting mathematical equations are equivalent to those in a synchronous rotating coordinate system with stator voltage vector orientation:

$$\begin{bmatrix} u_{sd} \\ u_{sq} \\ u_{rd} \\ u_{rq} \end{bmatrix} = \begin{bmatrix} R_s + pL_s & -\omega_s L_s & pL_m & -\omega_s L_m \\ \omega_s L_s & R_s + pL_s & \omega_s L_m & pL_m \\ pL_m & -\omega_{sl} L_m & R_r + pL_r & -\omega_{sl} L_r \\ \omega_{sl} L_m & pL_m & \omega_{sl} L_r & R_r + pL_r \end{bmatrix} \begin{bmatrix} i_{sd} \\ i_{sq} \\ i_{rd} \\ i_{rq} \end{bmatrix} \quad (2)$$

In the formula, u_{sd},u_{sq},u_{rd} and u_{rq} are the *d* and *q* axis components ofstator and rotor voltages, respectively. i_{sd},i_{sq},i_{rd} and i_{rq} are the *d* and *q* axis components of stator and rotor currents, respectively. L_s and L_r are the self-inductance of the stator and rotor windings, respectively. L_m is the mutual inductance between the stator and rotor windings. R_s and R_r are the stator and rotor resistances, respectively. ω_s and ω_{sl} are the operating angular frequency and slip angular frequency, respectively ($\omega_{sl} = S_{slip}\omega_s$, S_{slip} is the slip rate), and *p* is the differential operator.

2.3. Double-fed fan rotor side mathematical model

The stator resistance is relatively small compared with other parameters of an induction motor, such as reactance. Under steady-state conditions, the stator current is mainly influenced by the stator inductance and the load, while the effect of the stator resistance is negligible. Therefore, the stator resistance can be ignored to simplify the mathematical model. Under this assumption, the active and reactive powers of the doubly fed wind turbine can be approximately decoupled. When the rotor-side converter of the doubly fed wind turbine adopts stator-voltage-oriented vector control, the active and reactive output powers can be independently regulated by the d-axis and q-axis components of the rotor current, respectively. The mathematical equations of the rotor-side controller can be expressed as:

$$\begin{cases} u_{rd} = R_r i_{rd} + s L_r \dfrac{\mathrm{d}i_{rd}}{\mathrm{d}t} + \omega_{sl} \dfrac{L_m}{\omega_1 L_s} U_s - \omega_{sl} s L_r i_{rq} \\ u_{rq} = R_r i_{rq} + s L_r \dfrac{\mathrm{d}i_{rq}}{\mathrm{d}t} + \omega_{sl} s L_r i_{rq} \end{cases} \quad (3)$$

Where: ω_1 is the angular frequency of the grid voltage; σ is the magnetic leakage coefficient.

Further, the mathematical expressions of the active and reactive power at the stator side of the doubly fed wind turbine can be obtained as follows:

$$\begin{cases} P_s = \dfrac{3}{2} \dfrac{1}{L_s} u_s (\psi_{sd} - L_m i_{rd}) \\ Q_s = \dfrac{3}{2} \dfrac{1}{L_s} u_s (\psi_{sq} - L_m i_{rq}) \end{cases} \quad (4)$$

Where: ψ_{sd} and ψ_{sq} are the *d* and *q*-axis components of the stator flux.

Formula (4) shows that when the doubly fed wind turbine operates in a steady state, the stator active power P_s is mainly determined by the d-axis component i_{rd} of the rotor current, while the reactive power Q_s is mainly determined by the q-axis component i_{rq} of the rotor current.

Other detailed mathematical modeling of doubly fed wind turbines can be referred to in literature [27].

2.4. Explanation of oscillation mechanism of small interference

In a doubly fed wind turbine grid-connected system, the equivalent resistance on the rotor side can be expressed as $R_{rsc} = R_r / S_{slip}$ (R_r is the equivalent resistance of the rotor), where the slip ratio S_{slip} is:

$$s_{slip} = \frac{\omega_s - \omega_r}{\omega_s} \quad (5)$$

Where: ω_s is the operating angular frequency; ω_r is the rotor angular frequency.

When the system operates in the frequency range of the disturbance component and $\omega_s < \omega_r < \omega_{er}$, corresponding to the frequency band where the slip ratio $S_{slip} < 0$, the equivalent rotor-side resistance R_{rsc} becomes negative. When the absolute value of the rotor-side equivalent resistance is greater than the equivalent resistance of the stator side and its external circuit, the overall system exhibits a “negative resistance effect”. This effect leads to a gradual increase in line output voltage, current, and power dissipation oscillations, eventually causing system instability. Conversely, when the overall system is capable of dissipating the energy of the oscillatory components, a larger equivalent resistance provides a higher positive damping ratio, resulting in improved system stability. The mechanism of small-signal oscillations in the grid-connected doubly fed wind turbine system is illustrated in Figure 3.

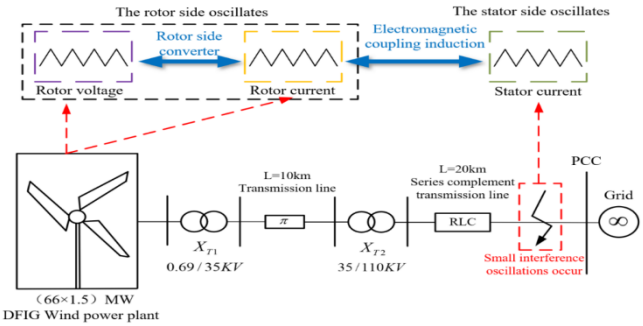

Figure 3. Propagation response diagram of small disturbance oscillation component

In order to ensure that the grid-connected doubly fed wind turbine system can maintain stable power quality even under small-signal oscillation conditions, the traditional control strategy for doubly fed wind turbines is relatively strict. Most existing strategies for suppressing small-signal oscillations involve designing a virtual damping controller (SSDC) based on the PI double closed-loop control of the wind turbine to mitigate system instability caused by small-signal oscillations. The overall control and suppression strategy structure of the rotor-side converter in the traditional doubly fed wind turbine system is shown in Figure 4.

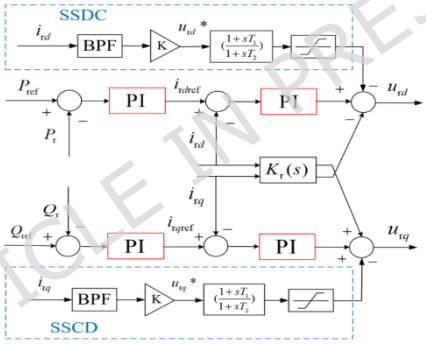

Figure 4. Structure diagram of PI control +SSDC control strategy for traditional doubly-fed fan rotor side converter

where ref denotes the reference quantity. At this stage, two issues need to be addressed in the study of small-signal oscillation suppression strategies for traditional grid-connected doubly fed wind turbine systems. On the one hand, during the actual operation of doubly fed wind turbines, the PI control loops in the turbine control system are unable to effectively suppress small-signal oscillations generated in the system and may even contribute to the progressive propagation of oscillation frequencies. On the other hand, random fluctuations in the overall wind power output result in real-time and uncertain variations in oscillation frequency, making it difficult to apply virtual damping controllers designed for a specific oscillation frequency in practice. Virtual damping controllers tuned for a fixed frequency are therefore often incapable of handling real-time variations in small-signal oscillation frequency. Consequently, based on the above two issues, this paper elaborates on the operating principles of the LADRC controller and the AQPR suppressor in Section III and adopts a combined LADRC+AQPR controller in

Section IV to block and suppress small-signal oscillations within the rotor-side converter of the doubly fed wind turbine, thereby addressing the problem of small-signal oscillations in the system.

3. Construct LADRC+AQPR joint controller

3.1. Building the LADRC Controller

In view of problems such as the stepwise propagation of small-signal oscillation frequency caused by variations under multiple operating conditions in a doubly fed wind turbine system connected to series-compensated transmission lines and the power grid, an LADRC controller is adopted in this section to replace the PI controller in the rotor-side current inner loop to track and suppress the small-signal oscillation frequency generated in the system. In this way, the coupling effect of oscillation frequency between the wind turbine controller and the series-compensated transmission line is effectively blocked. The LADRC controller does not require additional hardware devices and features strong robustness and simple parameter tuning, making it well suited for practical engineering applications. The structural diagram of the LADRC controller is shown in Figure 5.

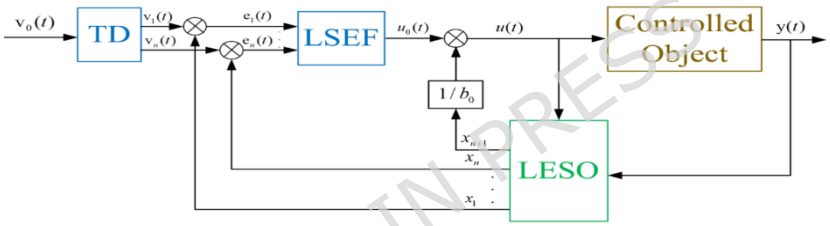

Figure 5. Structure diagram of LADRC

A.Tracking Differentiator (TD)

The role of the tracking differentiator (TD) is to provide two signals: a transition signal toward the target point and a differential signal. As an inertial element, the transition signal generates a smooth trajectory approaching the target point, during which no sudden change or overshoot occurs.

The principle of the TD can be derived from the closed-loop transfer function of a second-order system:

$$G=\frac{w_n^2}{s^2+2w_n xs+w_n^2} \qquad (6)$$

Where : ξ is the damping ratio; ω_n is the natural oscillation angular frequency.

When ξ =1, this is the ideal TD. At this time, the convergence rate of the system can be adjusted by adjusting the parameter ω_n, so that the set value can be reached faster.

From equation (6), the differential equation of the linear TD for a second-order system can be obtained as follows:

$$\frac{y_{md}}{u_{md}}=p^2 y_{md}+2rpy_{md}+r^2 y_{md} \qquad (7)$$

Set $\square_{md}=x_{1md}$ and $u_{md}=v_{md}$, where x_{1md} is the current state of the TD and

v_{md} is the target state. The relationship after setting is:

$$\begin{cases} px_{1md} = x_{2md} \\ x_{2md} = p^2 y_{md} = -2w_n x_{2md} - w_n^2 (x_{1md} - v_{md}) \end{cases} \quad (8)$$

Where: x_{1md} is the transition curve, which will always track the output v_{md}; x_{2md} is the differential of the transition curve.

B.Linear extended State Observer (LESO)

According to the d-axis equation of the rotor current controlling the active power output in equations (3) and (4), the derivative of both sides of the equation is simplified as follows:

$$\frac{d^2 i_{rd}}{dt^2} = \left(R_r w_s / s^2 L_r^2\right)\left(\frac{L_m}{w_1 L_s} U_s - s L_r i_{rq}\right) + \left(R_r^2 / s^2 L_r^2\right) i_{rd} \quad (9)$$
$$+ w_s \frac{d i_{rq}}{dt} + (1/s L_r)\frac{d u_{rd}}{dt} - R_r / \left(s^2 L_r^2\right) u_{rd}$$

The coupling terms and uncertainties that affect the controlled output in equation (9) are represented by f, and the second-order control object is obtained:

$$\frac{d^2 i_{rd}}{dt^2} = b u_{rd} + f \quad (10)$$

Where :b is the controller gain, $b=R_r/(\sigma^2 L_r^2)$; As a new state variable of the system, f can be regarded as the total disturbance inside and outside the system.

Then, the state equation of the system can be expressed as:

$$\begin{cases} px_1 = x_2 = \dfrac{d i_{rd}}{dt} \\ px_2 = x_3 + b u_{rd} = \dfrac{d^2 i_{rd}}{dt^2} \\ px_3 = h(\boldsymbol{x}, w) \\ y = x_1 = i_{rd} \end{cases} \quad (11)$$

Where : $x=[x_1,x_2,x_3]^T$is the state vector of the system; x_3 is the total disturbance f of the system, and its derivation is $h(x,w)$. w is the external disturbance of the system; u_{rd} is the control input signal output by LADRC to the rotor side. i_{rd} is the system output, which is also the input to the LESO and is controlled to quickly track the given reference value i_{rd_ref}.

The LESO is designed based on the linear system (11) to estimate and online compensate the total disturbance of a grid-connected doubly fed wind turbine system in real time. The state equation is as follows:

$$\begin{cases} p\hat{x}_1 = p\hat{x}_2 + l_1(x_1 - \hat{x}_1) \\ p\hat{x}_2 = p\hat{x}_3 + l_2(x_1 - \hat{x}_1) + b_0 u_{rd} \\ p\hat{x}_3 = l_3(x_1 - \hat{x}_1) \end{cases} \quad (12)$$

Where: $\hat{x}_1$ and $\hat{x}_2$ are the system state estimators; $\hat{x}_3$ is the estimator of the total disturbance caused by small disturbances. l_1, l_2 and l_3 are observer gain parameters. b_0 is the compensation factor of the LESO used to estimate the controller gain b. The parameters in the observer (12) are rounded as follows:

$$\begin{cases} l_1 = w_0 a_1 \\ l_2 = w_0^2 a_2 \\ l_3 = w_0^3 a_3 \\ a_i = \dfrac{(n+1)!}{i!(n+1-i)!} \end{cases} \quad (13)$$

The order n obtained from equation (11) is 2. In order to ensure the stability of the system and provide a good transition process, the characteristic equation of the third-order LESO can be expressed as follows:

$$l_0(s) = s^3 + a_1 w_0 s^2 + a_2 w_0^2 s + a_3 w_0^3 = (s + w_0)^3 \quad (14)$$

It can be seen that the observer $n+1$ gain coefficient β is simplified to the bandwidth ω_0 of the observer, and ω_0 usually has good robustness and adaptability, and has a wide adaptation range ,which makes it easy to debug.

C.Disturbance estimation compensation

According to the LESO estimation of the total disturbance inside and outside the system, the disturbance feedback quantity is used to dynamically compensate the small disturbance. Then, the final control quantity is formed to suppress the small-signal oscillation frequency in the rotor-side control system of the doubly fed wind turbine.

The LESO can observe the total system disturbance in real time when:

$$\hat{x}_3 \approx x_3 = f(i_{rd}, w(t)) \quad (15)$$

The control quantity u_{0_ref} of the final system is designed as:

$$u_{0\_ref} = u_0 - \frac{\hat{x}_3}{b_0} \quad (16)$$

Where: u_0 is the virtual control quantity; b_0 is the controller gain value in equation (10).

D.Linear State Error Feedback(LSEF)

Proper linear state error feedback can improve the anti-interference ability of the system and thus increase the stability of the controller. Equation (16) is substituted into the second-order state equation (10), and under the condition $b_0 \approx b$, it becomes the following new series integral system

$$y^{(2)}(t) = b u_0(t) \quad (17)$$

The voltage virtual control quantity u_0 in equation (17) is based on the following proportional and higher-order differential feedback control law:

$$u_0 = k_1(r_1 - \hat{x}_1) + k_2(r_2 - \hat{x}_2) + \cdots + k_n(r_n - \hat{x}_n) + r_{n+1} \quad (18)$$

In the formula, k_1 to k_n are controller gain parameters. And it has:

$$[r_1 r_2 \cdots r_n r_{n+1}] = [r \dot{r} \cdots r^{(n-1)} r^{(n)}] \quad (19)$$

E.Overall LADRC design

Where the LESO in the LADRC replaces the nonlinear ESO as:

$$\begin{cases} e = z_1 - y, f_e = \text{fal}(e, a, d) \\ \dot{z}_1 = z_1 + h(z_2 - b_1 e + b_1 u_q) \\ \dot{z}_1 = z_2 + h(-b_2 f_e) \end{cases} \quad (20)$$

Where: h is the integral step; β_1 and β_2 are adjustable observer gain coefficients. b_1 is the compensation factor of the nonlinear state observer; $\_1$ is the state estimate of the tracking output $\_;z_2$ is the estimate of the total disturbance of the system. ffal(e,α,δ) is a nonlinear power function:

$$\text{fal}(e, a, d) = \begin{cases} \dfrac{e}{d^{1-a}}, |e| \le d \\ |e|^a \operatorname{sgn}(e), |e| > d \end{cases} \quad (21)$$

Where: α is a power parameter, usually with a value of 0.5; δ is the length of the linear segment interval, which can be the sampling step; sgn(e) is the sign function.

Using the fastest feedback function fhan, the following nonlinear state error feedback is constructed:

$$\begin{cases} e_1 = v_0 - z_1 \\ u_0 = -\text{fhan}(e_1, c, r, h_1) \end{cases} \quad (22)$$

In this equation, e_1 represents the tracking error of the system; the parameter c is a nonlinear feedback gain introduced to achieve a trade-off between the system response speed and chattering suppression; r controls the response speed of the tracking differentiator to input signal variations and is generally chosen to be on the same order of magnitude as the desired closed-loop bandwidth; h_1 is the sampling period.

The fhan function can be expressed as:

$$\begin{cases} \text{fhan} = -\begin{cases} r * \operatorname{sgn}(a), |a| > d \\ ra / d, |a| \le d \end{cases} \\ a = \begin{cases} x_2 + (a_0 - d)\operatorname{sgn}(y)/2, |y| > d_0 \\ x_2 + y / h_1, |y| \le d_0 \end{cases} \\ a_0 = \sqrt{d^2 + 8r|y|} \\ y = x_1 + h_1 x_2 \\ d_0 = h_1 d \\ d = rh_1 \end{cases} \quad (23)$$

In this equation, y,α, and α_0 denote the internal variables of the fhan function. The parameters dd =rh1 and d0 =hd define the nonlinear piecewise thresholds that separate the linear and nonlinear error regions, ensuring continuity and robustness of the control law near the error zero-crossing. The parameter configuration is consistent with the standard design guidelines of active disturbance rejection control (ADRC) theory.

For the establishment of the above LADRC controller, its operating mechanism lies in that, when the RSC adopts stator-voltage-oriented vector control, according to (3), the rotor-side closed-loop controller regulates the rotor current $\dot{I}_{rd}$ and $\dot{I}_{rq}$ by controlling the d-axis and q-axis components of the rotor voltage, thereby stabilizing the output power of the DFIG. Therefore, the linear ADRC control

principle for the doubly fed wind turbine in this paper can be summarized as follows: the rotor-side outer loop compares the reference values of the turbine output active and reactive power with the measured values, and then generates the d-axis and q-axis reference values of the rotor current through PI control as the inputs of the inner loop. Subsequently, by regulating the d-axis and q-axis components of the rotor voltage, decoupled control of the active and reactive power of the doubly fed wind turbine is achieved. In Fig. 5, the linear ADRC replaces the conventional PI controller in the inner loop. The tracking differentiator (TD) arranges the transition process for the d-axis component of the rotor current i_{rd}, avoiding excessive overshoot during system start-up and obtaining its differential signal. The target error and differential error are then input into the LESO. As the core of ADRC, the LESO observes the total disturbance of each system state based on the input and output data. The linear state error feedback (LSEF) effectively suppresses disturbances and enhances system stability through the designed proportional and higher-order differential feedback control law. Finally, according to (16), a compensation process is applied to the feedback control quantity, enabling dynamic compensation of subsynchronous disturbances, suppression of SSCI, and generation of the final control signal u_{rd}.

The purpose is to improve the tracking performance of the rotor-side control system of the doubly fed wind turbine with respect to the target signal while blocking the transmission path of small-signal oscillation frequency, thereby satisfying the performance requirements for stabilized control of the rotor-side converter of the doubly fed wind turbine [25].

3.2. Construct AQPR suppressor

The LADRC controller can block the propagation path of small-signal oscillation frequency from the inner current loop of the rotor-side converter of the doubly fed wind turbine; however, a certain level of small-signal oscillation frequency may still exist in the control current signals i_{rd} and i_{rq}, introduced by the cross-coupling terms of the rotor-side converter. Therefore, simply replacing the PI controller in the inner loop of the rotor-side converter with the LADRC controller cannot completely suppress small-signal oscillations in the control system. To ensure stable power quality of the entire wind turbine system, this paper further employs an AQPR suppressor to track and suppress small-signal oscillation frequencies in the cross-control current signals i_{rd} and i_{rq}.

The transfer function of a conventional quasi-proportional resonant (QPR) suppressor is given as follows:

$$G(s)=K_p+\frac{2K_r\omega_c s}{s^2+2\omega_c s+\omega_v^2} \quad (24)$$

Where K_p is the proportional gain coefficient, K_r is the integral gain coefficient, ω_c is the cut-off frequency, and ω_v is the center frequency.

Traditional QPR suppressors also belong to the category of SSDC controllers. They adjust a fixed center frequency ω_v to match the small-signal oscillation frequency ω_{er}, so that the oscillation component can be accurately tracked without amplitude gain or phase offset, and the value of ω_v is typically determined based

on historical experience or offline data. However, in practical operation of the wind turbine system, ω_{er} varies in real time. For traditional QPR suppressors, the inability to adapt to real-time variations in oscillation frequency makes their suppression performance difficult to guarantee [26]. Therefore, this section designs an AQPR suppressor by employing an ITD algorithm capable of extracting ω_{er} in real time and combining it with a frequency-locking update module that can lock and update the center frequency ω_v of the QPR suppressor. As a result, the rotor-side control system of the doubly fed wind turbine can maintain good control performance even when ω_{er} changes dynamically.

A. ITD algorithm

The selection of a small-signal oscillation frequency extraction algorithm with low computational complexity, a simple structure, and good performance is beneficial for real-time monitoring and extraction of oscillation frequency signals. The ITD algorithm is widely used in signal processing due to its fast convergence speed and good error performance. In this paper, the ITD algorithm is employed to provide small-signal oscillation frequency information for the traditional QPR suppressor.

For the original signal $X_t(t \geq 0)$, a low-frequency oscillation signal extraction operator ρ is defined, which separates the signal into a low-frequency oscillation component L_t and a high-frequency component H_t, and X_t can be expressed as:

$$\begin{cases} X_t = rX_t + (1-r)X_t = L_t + H_t \\ L_t = rX_t \\ H_t = (1-r)X_t \end{cases} \quad (25)$$

Determine all extreme points in the original signal X_t interval X_k (k=1,2,3,...) and the corresponding time τ_k, as shown in Figure 6.

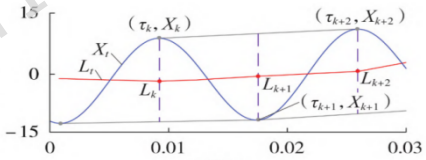

Figure 6. Decomposition principle

Suppose that L_t and H_t exist in the interval $[0, \tau_k]$, and X_t exists in $[0, \tau_{k+2}]$. Assume that L_t is an affine linear approximation of X_t over the interval $(\tau_k, \tau_{k+1}]$, i.e., $L_t = mX_t + n_t$ where $t \in (\tau_k, \tau_{k+1}]$. Then, within the interval $(\tau_k, \tau_{k+1}]$, a low-frequency signal extraction operator ρ can be defined as:

$$rX_t = L_t = L_k + \frac{L_{k+1} - L_k}{X_{k+1} - X_k}(X_t - X_k) \quad t \in (t_k, t_{k+1}] \quad (26)$$

Where $L_k = L(\tau_k)$. L_{k+1} determines the low-frequency signal, resulting in:

$$L_{k+1} = 0.5\left[X_k + \frac{t_{k+1} - t_k}{t_{k+2} - t_k}(X_{k+2} - X_k)\right] + 0.5X_{k+1} \quad (27)$$

After signal decomposition, the remaining high-frequency signal H_t is defined, and its corresponding extraction operator ε is given as follows:

$$H_t = X_t - L_t = (1 - r)X_t = eX_t \quad (28)$$

Let the sampling frequency of the algorithm be 1000 Hz. The three-phase current signal of the doubly fed wind turbine output in the Cartesian coordinate system is used to identify oscillations. After the algorithm is decomposed, the low-frequency component L_t corresponds to the small-signal oscillation frequency component, while the high-frequency component H_t corresponds to the fundamental wave component.

Because the original ITD algorithm needs to store a large amount of data to retain continuous extreme points within the time window, its real-time computational performance is limited. For this reason, an improved iterative operation is adopted to ensure real-time performance and achieve better extraction accuracy.

As can be seen from Equation (25), the key point L_k of the oscillatory component is determined by the extreme point of the original signal X_k. For two consecutive extreme points satisfying Equation (29), there must exist a zero crossing (t_z, L_z), where $t_z \in (\tau_k, \tau_{k+1})$], and the corresponding value X_z can be obtained from Equation (30).

$$L_{k+1} L_k < 0 \quad (29)$$

$$L_z = L_k + \frac{L_{k+1} - L_k}{X_{k+1} - X_k}(X_z - X_k) = 0 \quad (30)$$

Since the original curve is monotonic between two extreme points, the horizontal coordinate of X_z can be calculated, that is, the horizontal coordinate t_z of the zero crossing of the oscillation component.

From the horizontal coordinates t_{z-1} and t_z of the two consecutive zero-crossing points of the oscillation curve, the oscillation frequency ω_{er} can be obtained as:

$$w_{er} = \pi / (t_z - t_{z-1}) \delta t_0 \quad (31)$$

Where: δt_0 is the sampling time of X_t, and ω_{er} is updated once every time a zero crossing is detected. The ITD pseudocode is shown in Figure 7.

Algorithm 1 Improved ITD-Based Oscillation Frequency Estimation

Require: Sampled signal $x[n]$, sampling period T_s
Ensure: Estimated oscillation frequency ω_r

```
Initialize extrema list E ← ∅
Initialize frequency list F ← ∅
for each new sample x[n] do
    Detect extrema of x[n] and update E
    if |E| < 3 then
        continue
    end if
    Take last three extrema (t_{k-1}, x_{k-1}), (t_k, x_k), (t_{k+1}, x_{k+1})
    Compute low-frequency components L_k, L_{k+1}
    if L_k · L_{k+1} < 0 then
        Interpolate zero-crossing time t_c
        Compute ω_r = π/(t_c − t_{k-1})
        Append ω_r to F
        Optionally smooth ω_r
    end if
end for
return the latest ω_r
```

Figure 7 Pseudocode for the ITD Algorithm

The improved ITD algorithm, after undergoing iterative operation, significantly reduces the amount of data required. Compared with the commonly used Prony, ERA, and other oscillation extraction algorithms with complex matrix operations, its computational burden is smaller, and it is more suitable for real-time monitoring and extraction. Subsequently, the monitoring and extraction performance of the Prony algorithm, ERA algorithm, and improved ITD algorithm are compared, respectively, with the input of certain measured signals.

The time window of each algorithm is uniformly selected as 100 ms, and the sampling frequency is 1000 Hz. The measured signal input is:

$$\begin{cases} y = 100\cos(2\pi \times 60t) + 10\cos(2\pi \times f_{er}t) \\ w_{er} = 2\pi \times f_{er} \end{cases} \quad (32)$$

In the formula, f_{er} is the frequency signal that varies in the range of 4 to 48 Hz. Figure 8 shows the frequency tracking performance of the Prony, ERA, and ITD algorithms, in which f_P, f_E and f_I respectively represent the oscillation frequencies identified by the Prony, ERA, and ITD algorithms. It can be seen that the three methods can track the oscillation frequency, and the calculation result of the ITD algorithm is more accurate.

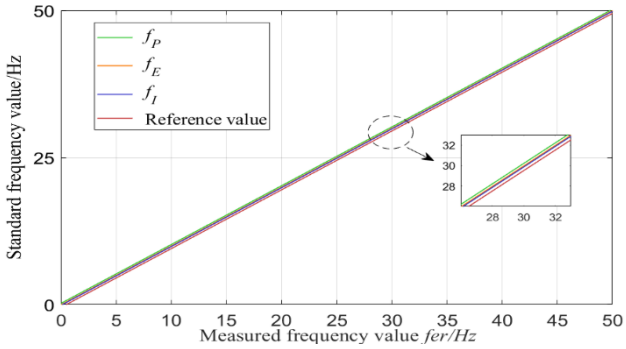

Figure 8. Comparison of frequency tracking performance of three oscillatory identification algorithms

In practical applications, a certain delay exists when using the improved ITD algorithm to adjust the center frequency ω_v of the QPR suppressor, which mainly arises from hardware computation and frequency measurement delays. Therefore, based on historical oscillation data and simulation results, it can be observed that setting the maximum delay of the ITD algorithm to t_0=101 ms can effectively mitigate the above delay issue.After the delay t_0, the ITD algorithm can accurately extract the oscillation frequency, and the frequency is then locked in real time through the subsequent frequency-locking update module to update the center frequency ω_v of the QPR suppressor, which significantly improves its suppression performance.

B. Frequency locking update module

Ideal QPR controllers may lead to system stability problems when implemented in practical systems due to the infinite quality factor resulting from their infinite gain [27]. In addition, when the frequency of the input signal slightly deviates from the base frequency of an ideal PR controller, its gain is significantly reduced, which may prevent the controller from properly regulating the reference signal.In practical grid-connected inverter systems, the grid voltage frequency is not constant but fluctuates within a certain range. As a result, ideal PR controllers cannot effectively cope with grid frequency deviations and therefore fail to eliminate steady-state errors, which limits their application in practical inverter-based grid-connected systems.To address this issue, non-ideal QPR controllers are introduced to increase system damping [28,29], and the transfer function of the non-ideal QPR controller is given in Equation (32).

$$G_{QPR}(s) = K_P + \frac{2K_r w_c s}{s^2 + 2w_c s + w_v^2} \quad (33)$$

Where$\omega_c$is the system cut-off frequency, K_r is the gain coefficient, and ω_v is the resonant frequency. Based on the transfer function of the QPR controller, the corresponding Bode plot is drawn and compared with that of the ideal PR controller.From Figure 9, it can be observed that the introduction of the cut-off frequency enables the PR controller to obtain high gain over a wide bandwidth, thereby reducing its sensitivity to grid frequency variations. Although the introduction of system damping reduces the gain of the non-ideal PR controller at the fundamental frequency, the gain remains sufficiently large to achieve a near-zero steady-state error.This ensures that the gain provided by the QPR controller is not significantly affected by grid frequency fluctuations, allowing the system to operate in a safe and stable manner.

According to Equation (32) and Figure 9, the amplitude gain of the controller is positively correlated with the value of K_r. When K_r is fixed, the amplitude and phase characteristics of the quasi-resonant controller tend to become smoother with increasing ω_c; that is, the value of ω_c is negatively correlated with the degree to which $G(s)$ is affected by frequency variations.However, regardless of the variations

in $\omega_c$and K_r, once ω_v is determined, the quasi-resonant controller exhibits the best tracking performance at that frequency. Therefore, it is feasible to use the quasi-resonant controller to regulate the small-signal oscillation (SSO) components in the DFIG system.However, the quasi-resonant controller can only effectively control AC signals at specific frequencies, and when the input signal frequency deviates from the resonant frequency ω_v, its control performance deteriorates significantly. Considering the variation of the SSO frequency, an adaptive algorithm is required to enhance the performance of the quasi-resonant controller.

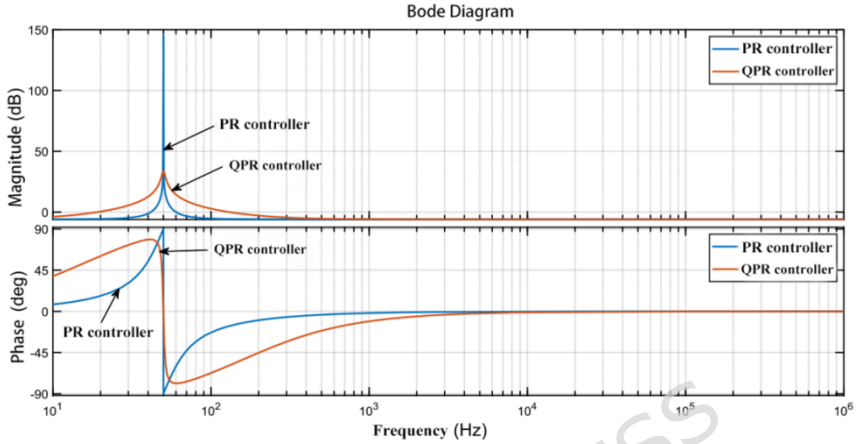

Figure 9. Bird's plot of PR and QPR controllers

This article employs the aforementioned QPR controller to ensure compensation at the fundamental frequency. In addition, a frequency-locking update module is integrated into the QPR controller, as shown in Figure 10. The basic principle is to extract the small-signal oscillation frequency using the ITD algorithm.Subsequently, the frequency-locking update module locks and updates the extracted small-signal oscillation frequency and replaces the center frequency ω_v of the QPR suppressor in real time. The updated frequency is then used as the input of the QPR controller to track the small-signal oscillation frequency and eliminate oscillations.

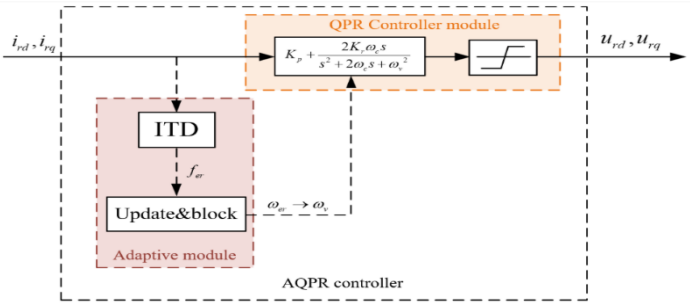

Figure 10. Overall structure of AQPR suppressor

Since the ITD algorithm is susceptible to sudden changes in frequency amplitude during the frequency identification process, which may result in obvious output jumps, the frequency-locking module of the AQPR suppressor is designed to filter out the jump components in the oscillation frequency ω_{er} extracted by the ITD algorithm. Subsequently, it replaces the output ω_{er} with the center frequency ω_v of the AQPR suppressor in real time. The workflow of the AQPR suppressor for

adaptively adjusting the oscillation frequency is described as follows: when the small-signal oscillation frequency ω_{er} falls within the small-signal oscillation frequency band $[\omega_{l\_er},\omega_{h\_er}]$ and remains unchanged for a duration of τ_t (where τ_t is generally selected as 50 ms, corresponding to 2.5 fundamental frequency cycles), the frequency-locking update module updates the center frequency ω_v to ω_{er} and keeps it unchanged. The value of ω_{er} ranges from 2π x (4Hz to 48 Hz).

4. Inhibition strategies of joint control by LADRC and AQPR

4.1. Integrated joint controller control structure

In order to optimize the tracking performance of the rotor-side converter of the doubly fed wind turbine for the DC component and to enhance the suppression performance of small-signal oscillation frequency, the control model structure of the LADRC + AQPR joint controller proposed in this paper is shown in Figure 11.

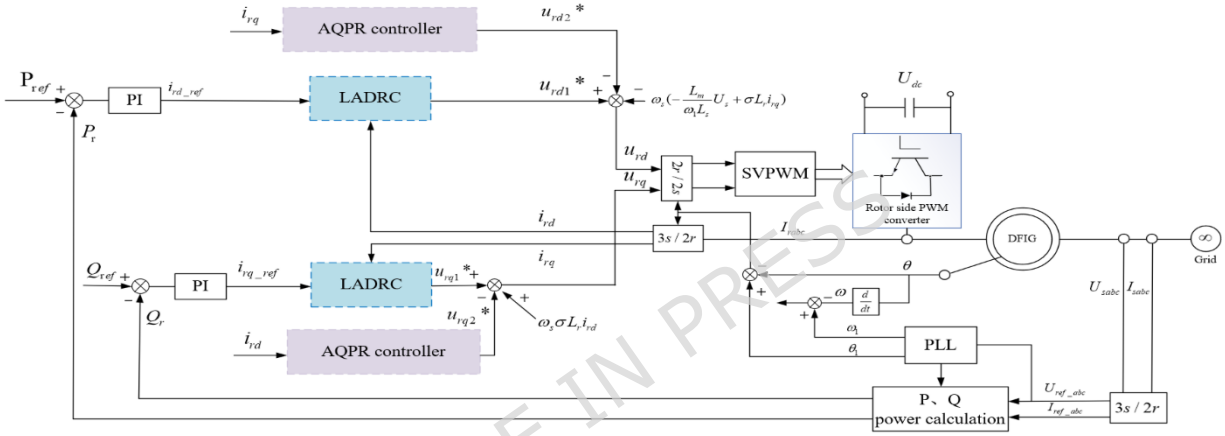

Figure 11. Structure diagram of control system of LADRC+AQPR joint controller based on rotor side of doubly-fed fan

4.2. Integral joint controller parameter tuning

A. LADRC parameter setting

The control structure of the LADRC controller is shown in the blue block of Fig. 11, and its parameters are tuned using a bandwidth-parameterization-based LADRC design approach.

Compared with nonlinear ADRC [22], whose tuning process involves the nonlinear functions fal(·) and fhan(·) with inflection points, a relatively large number of tuning parameters, and high tuning difficulty, the parameter tuning procedure of the LADRC controller is considerably simplified. In contrast to the nonlinear ADRC controller, the LADRC controller only requires the adjustment of four parameters, namely k_1 ,k_2,b_0, and ω_0 .Among them, $\omega_0$denotes the bandwidth parameter of the extended state observer (ESO), and its selection directly determines the dynamic response speed and estimation accuracy of disturbance estimation. During the tuning process, ω_0 is first selected according to the desired closed-loop bandwidth of the system and is typically set to 3–5 times the bandwidth of the inner current loop, so as to achieve rapid estimation and compensation of small disturbances and parameter uncertainties while ensuring system stability.Based on this, the ESO gains k_1 and k_2 are determined according to the standard LADRC

bandwidth configuration relationships to guarantee the dynamic convergence of the observer estimation error.

The compensation factor is tuned to be close to the true value of the control gain $R/(\sigma^2 L_r^2)$ and is then fine-tuned within a small range in simulation to meet the requirements of closed-loop stability and transient response.With the above parameter configuration, the LADRC achieves a sufficient stability margin, good disturbance rejection performance, and interpretable physical meaning in the inner current loop, thereby laying a foundation for the subsequent design of the combined control strategy.

B. AQPR suppressor parameter tuning

The control structure of the AQPR suppressor is shown in the purple block diagram in Figure 11.

Since the ITD algorithm can extract the oscillation frequency in real time and the center frequency ω_v of the AQPR suppressor can be tracked and updated through the frequency-locking update module, it is only necessary to set the proportional gain K_p, integral gain K_r, and parameter ω_c for the AQPR suppressor.According to the control principle, the parameter ω_c is selected as a small value (such as $2\pi\times0.1$, $2\pi\times0.5$, $2\pi\times1$) to ensure that the bandwidth around the oscillation frequency is kept within a narrow range, thereby preventing adverse effects caused by fluctuations in small-signal oscillation frequency.Therefore, the only parameters that require tuning optimization are K_p and K_i. In the following, the control variable method is adopted to tune each parameter of the AQPR suppressor.

a) Proportional gain K_p parameter tuning

For the proportional gain $K_p$parameter, K_r=100 and ω_c=314 are fixed, and $K_p$values are selected as 0.1, 1, and 10. The corresponding Bode frequency characteristics are shown in Figure 12.

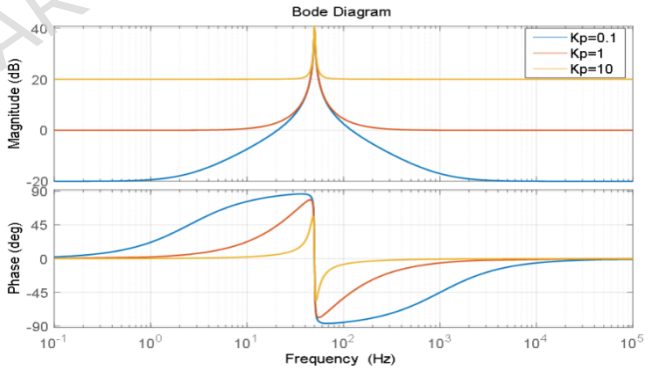

Figure 12. Bode diagram of proportional gain K_p parameter change of AQPR suppressor

As can be seen from Figure 12, with the increase of the proportional gain K_p of the AQPR suppressor, the overall phase margin and frequency bandwidth are influenced by variations in K_p. However, the amplitude at the fundamental frequency remains unchanged and only increases at non-fundamental frequencies, while the corresponding bandwidth decreases as K_p increases. Therefore, as K_p increases, the anti-interference capability of the system is enhanced. Nevertheless,

K_p cannot be increased indefinitely, as an excessively large value may introduce additional oscillations and adversely affect overall system stability. Based on the above analysis and the requirements of this experimental study, the proportional gain K_p is set to 6.5.

b) Integral gain K_r *parameter tuning*

For the integral gain parameter K_r ,with K_p=10 and ω_c=314,the values of K_r are selected as 10, 100 ,and 1000, and the corresponding Bode frequency characteristics are shown in Figure13 .

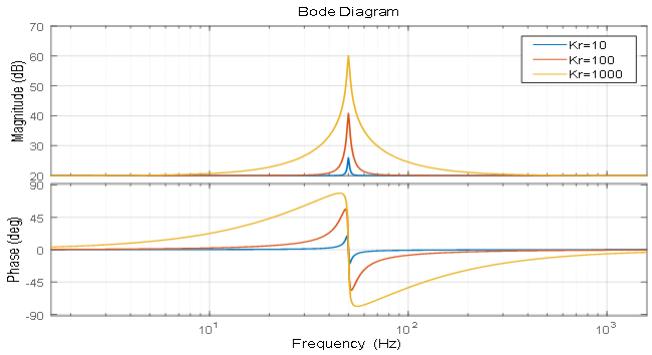

Figure 13. Bode diagram of AQPR suppressor integral gain K_r parameter change

As can be seen from Figure 13, with the increase of the integral gain K_r of the AQPR suppressor, the overall amplitude of the suppressor increases continuously, and its stability is correspondingly enhanced, while the frequency bandwidth of the suppressor remains unchanged. However, an excessive increase in K_r may lead to the amplification of harmonic components. Therefore, K_r should be selected appropriately to ensure a sufficiently large gain at the center frequency while providing a certain attenuation of small-signal oscillation frequencies. Based on the above analysis and the requirements of this experimental study, the integral gain K_r is set to 120.

Based on the above analysis, the parameter tuning of the controller in this paper mainly follows the principle of combining bandwidth configuration with stability margin constraints. For the LADRC controller, the ESO bandwidth parameter (ω_0) is first selected based on the desired dynamic performance of the system (typically 3 to 5 times the bandwidth of the inner current loop), and the ESO gain parameters are determined according to the bandwidth configuration relationship to ensure a balance between disturbance estimation speed and system stability. For the AQPR suppressor, the proportional gain (K_p) and integral gain (K_r) are mainly adjusted to achieve high suppression gain near the target oscillation frequency while ensuring the system maintains sufficient stability margin.

5. Simulation verification

In order to verify the ability of the LADRC+AQPR joint controller to suppress small-signal oscillations without affecting the steady-state and transient stability performance of the doubly fed wind turbine, this paper establishes a simulation model of a doubly fed wind turbine system connected to the grid through series-

compensated transmission lines using MATLAB R2023b and Simulink R2023b (MathWorks). The parameters of the doubly fed wind turbine, transmission line, and control system are listed in Table 1.

Table 1. Initial values of circuit and control parameters of grid-connected douply-fed fan system

argument	Numerical value
Operating power /MW	100
Rated frequency /Hz	50
switching frequency/Hz	5000
Stator operating power Us/V	690
Dc voltage Udc/kV	1.15
Number of poles	2
Stator resistance Rs/p.u.	0.0048
Stator leakage reactance Xls/p.u.	0.17
Rotor resistance Rr/p.u.	0.0064
Rotor leakage reactance Xlr/p.u.	0.24
Field reactance Xm/p.u.	3.34
Transmission line resistance Rl/p.u.	0.02
Transmission line reactance Xl/p.u.	0.59
Transformer T1 reactance XT1/ p.u.	0.14
Transformer T1 reactance XT2/ p.u.	0.23
Line series complement 10%	161uF
GSC voltage outer loop	K_p=0.2 K_i=40
GSC current inner loop	K_p=0.5 K_i=30

5.1. LADRC controller operation performance analysis

In order to verify that the LADRC controller does not affect the stable operation capability of the overall grid-connected doubly fed wind turbine system, the control performances of the LADRC and PI controllers are simulated and compared. Initially, the wind speed is set to v=10m/s, and the series compensation level of the transmission line is K_c=10%. At 3 s, the wind speed of the wind farm is changed from 10 m/s to 12 m/s; at 6 s, the series compensation level K_c is increased from 10% to 18%. Through simulation studies, the output of the rotor-side inner-loop control signal urd1* is compared between the LADRC and PI controllers, and the corresponding results are shown in Figure 14.

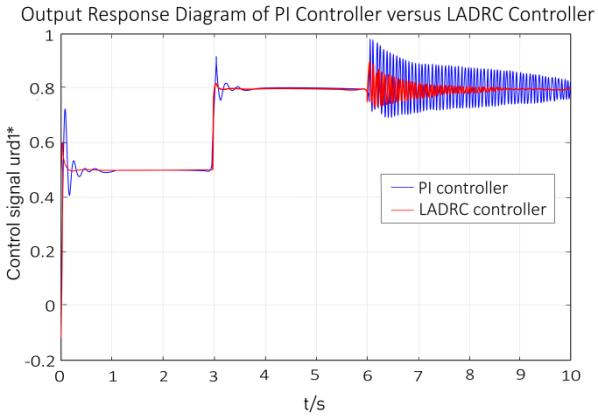

Figure 14. Output response of PI controller and LADRC controller to control signal urd1*

As can be observed from Figure 14, when the wind speed increases at 3 s, the

LADRC controller exhibits less overshoot and a more stable final output of the control signal urd1* compared with the PI controller. This is because, in the initial stage of PI control, the error feedback is directly used to eliminate the error, which leads to an excessively large initial control action and results in overshoot. Furthermore, when the series compensation level of the transmission line increases at 6 s, the small-signal oscillations in the control signal urd1* generated by the LADRC controller are effectively suppressed, allowing the control signal to converge rapidly. In contrast, the PI controller requires a longer time to achieve oscillation suppression. Therefore, the experimental results demonstrate that the LADRC controller can not only block the transmission path of small-signal oscillations but also improve the tracking performance of the target control signal.

Table 2. Performance Comparison of PI and LADRC Inhibitor Output Signal Urd2

Metric	PI Controller	LADRC Controller
L1：0-1s：Overshoot (%)	42.537	12.434
L1：Settling time (±2%) (s)	0.403	0.132
L2：Steady-state error e_{ss}	-0.0143	-0.0025
L1：Standard deviation σ	0.068	0.033
L2：Overshoot (%)	11.232	2.253
L2：Settling time (±2%) (s)	0.271	0.052
L2：Steady-state error e_{ss}	0.043	0.012
L2：Standard deviation σ	0.038	0.012
L3：Oscillation amplitude	0.112	0.063
L3：Equivalent damping ratio ζ	0.011	0.209
L3：Steady-state error e_{ss}	-0.012	-0.003
L3：Standard deviation σ	0.067	0.023

5.2. AQPR suppressor operation performance analysis

In order to verify the ability of the AQPR suppressor to track and suppress small-signal oscillations in real time when the oscillation frequency varies dynamically, the traditional QPR suppressor with a fixed center frequency is compared with the AQPR suppressor proposed in this paper. The experimental design is as follows: under the conditions of a fixed wind speed v=10m/s and a series compensation level of the transmission line K_c=10%, small-signal oscillations with a harmonic frequency of 25 Hz are injected into the cross-control current signals Δi_{rd} and Δi_{rq} at 3 s. At t=6s, the injected harmonic frequency is changed to 34 Hz. The output response of the final control signal urd2* is shown in Figure 15. It should be noted that the center frequency of the traditional QPR suppressor is fixed at 25 Hz.

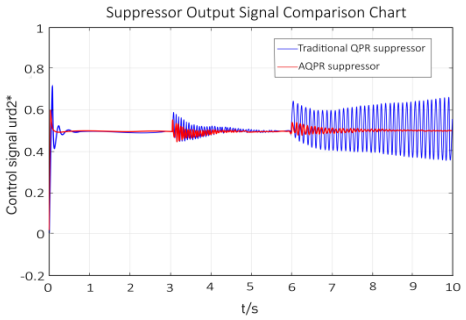

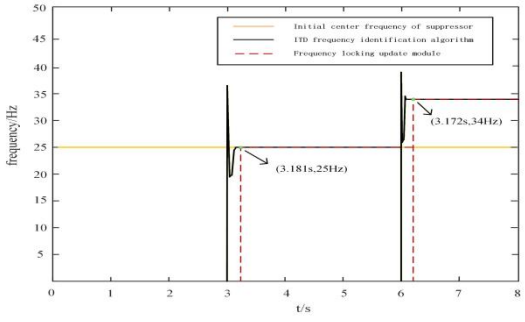

(a) Output response diagram of control signal urd2* with two different suppressors

(b)Oscillation detection with harmonic freq. 25 - 34Hz for frequency - locked module

Figure 15. Experimental comparison of 2 suppressors at 25Hz -34Hz low - interference frequencies

As can be seen from Figure 15(a), when the small-signal oscillation frequency in the inner-loop cross-control signal $\square_{rd}$ and $\square_{rq}$ on the rotor side of the doubly fed wind turbine is 25 Hz, both suppressors are capable of effectively suppressing the small-signal oscillations. When the oscillation frequency increases to 34 Hz, the traditional QPR suppressor loses its suppression capability because its center frequency significantly deviates from the small-signal oscillation frequency. In contrast, when the AQPR suppressor is applied, its center frequency can be locked and updated in real time according to the variation of the oscillation frequency, thereby enabling effective suppression of time-varying small-signal oscillations in the control signal. Meanwhile, as shown in Figure 15(b)(c), the frequency-locking update module can effectively filter out output jumps in the estimated oscillation frequency after identification by the ITD algorithm, thus reducing unnecessary disturbances to the control system. In addition, the frequency-locking update module in the AQPR suppressor maintains the previous frequency value after the oscillations subside, which ensures stable system operation under this condition and demonstrates the superior control performance of the AQPR suppressor.

Table 3. Performance Comparison of QPR and AQPR Suppressor Output Signal urd2

Metric	QPR Controller	AQPR Controller
L1(0-1s)□Overshoot (%)	27.573	14.132
L1□Settling time (±2%) (s)	0.396	0.087
L1□Steady-state error e_{ss}	-0.014	-0.003
L1□Standard deviation σ	0.071	0.033
L2(3-5s)□Overshoot (%)	14.292	4.711
L2□Settling time (±2%) (s)	1.504	1.145
L2□Steady-state error e_{ss}	0.006	-0.002
L2□Standard deviation σ	0.024	0.011
L3(6-10s)□Oscillation amplitude	0.132	0.022
L3□Equivalent damping ratio ζ	0.274	0.281
L3□Steady-state error e_{ss}	-0.006	-0.002
L3□Standard deviation σ	0.074	0.011

5.3. Suppression performance analysis of LADRC+AQPR joint controller

In this section, the LADRC+AQPR joint controller (referred to as the new controller in the simulation results) is compared with the traditional PI control + SSDC controller[29] (referred to as the conventional controller in the simulation results) proposed in the literature for small-signal oscillation suppression under multiple operating conditions, including different wind speeds v and series compensation levels K_c. The operating conditions are listed in Table 4.

Figures 16, 17, 18, and 19 present the comparative waveforms of the three-phase stator currents, DC-bus voltage, active power, and reactive power output of the doubly fed induction generator (DFIG) under operating condition A, respectively. It can be observed that although both controllers exhibit good convergence performance, the LADRC+AQPR combined controller achieves better dynamic performance than the traditional controller in all four output waveforms, with faster convergence speed and smaller overshoot.

Figures 21 and 22 show the comparison of the three-phase stator currents and DC-bus voltage of the DFIG under operating condition B. Combined with Table 5, it can be seen that the three-phase stator currents under the traditional controller exhibit slight oscillatory convergence deviation; however, convergence can still be achieved after a relatively long suppression process. This is because the small-signal oscillation frequency only slightly deviates from the center frequency of the SSDC controller. In contrast, the system controlled by the LADRC+AQPR combined controller maintains good suppression performance, with faster convergence speed and smaller overshoot than the traditional controller. Figures 23 and 24 present the comparisons of active and reactive power outputs under operating condition B for the traditional controller and the PI+SSDC controller. As shown in Table 5, the active and reactive power outputs of the LADRC+AQPR combined controller are also superior to those of the traditional controller.

Figures 26 and 27 show the comparison of the three-phase stator currents and DC-bus voltage of the DFIG under operating condition C. It is evident that the system stability of the traditional PI+SSDC controller deteriorates significantly. When KcK_cKc increases to 35%, the traditional PI+SSDC controller, whose center frequency is fixed at 20 Hz, fails to suppress the 36 Hz small-signal oscillation, resulting in oscillatory divergence and loss of system stability. Figures 28 and 29 present the comparison of active power output under operating condition C for the traditional PI+SSDC controller. As can be seen from Table 5, the advantage of the LADRC+AQPR combined controller over the traditional controller in terms of active power output becomes even more pronounced.

Figures 20, 25, and 30 show the frequency-locking module updates of the LADRC+AQPR combined controller under operating conditions A, B, and C, respectively. It can be observed that the LADRC+AQPR combined controller effectively performs real-time frequency extraction, locking, and updating, thereby enabling rapid suppression of small-disturbance oscillations in the DFIG grid-connected system.

Table 4. Working conditions under different wind speed v and series complement K_c

Working condition	Wind speed v (m/s)	Initial line series complement K_c (%)	Line series complement after change K_c (%)
A	9	10	28
B	11	10	32
C	13	10	35

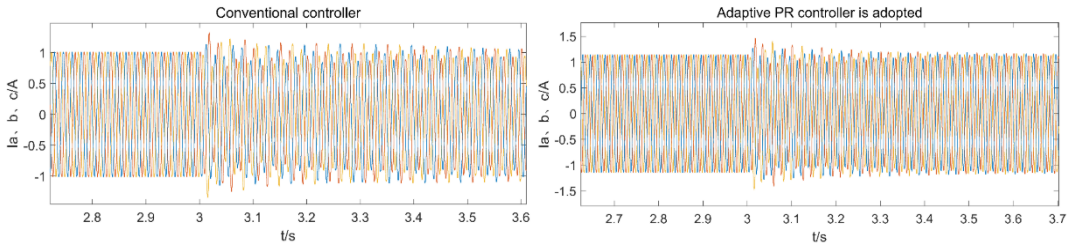

Figure 16 Working Condition A: Three-phase stator current output waveform of doubly-fed fan

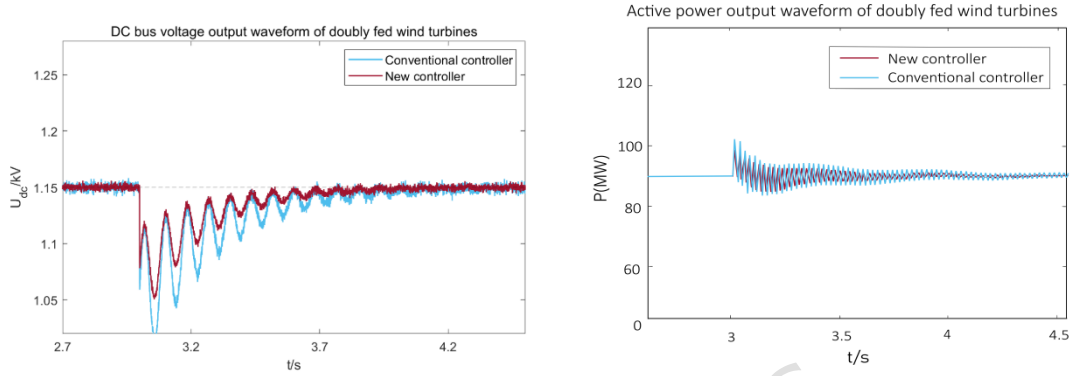

Figure 17 Working Condition A: Bus voltage output waveform of a doubly fed generator

Figure 18 Working Condition A:Active power output waveform of a doubly fed generator

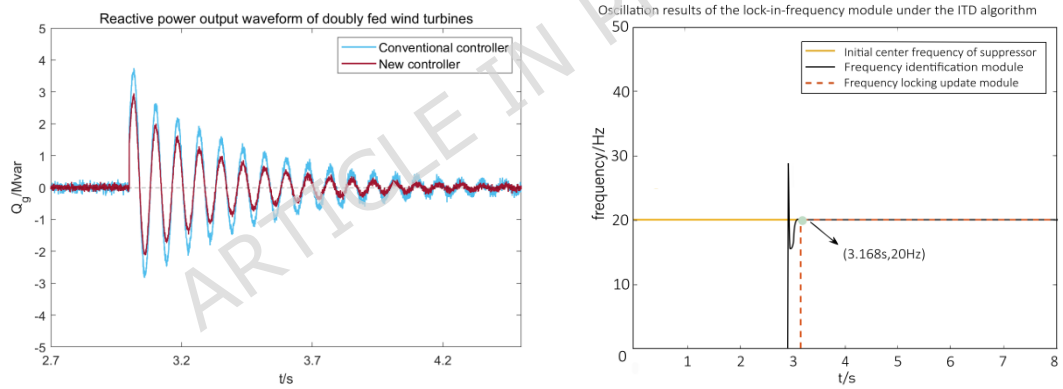

Figure 19 Working Condition A: Qg output waveform of a doubly fed generator

Figure 20 Working Condition A: Small interference oscillation detection results

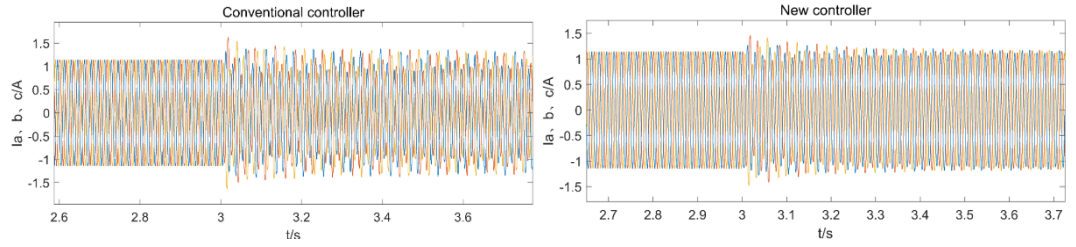

Figure 21 Working Condition B: Three-phase stator current output waveform of doubly-fed fan

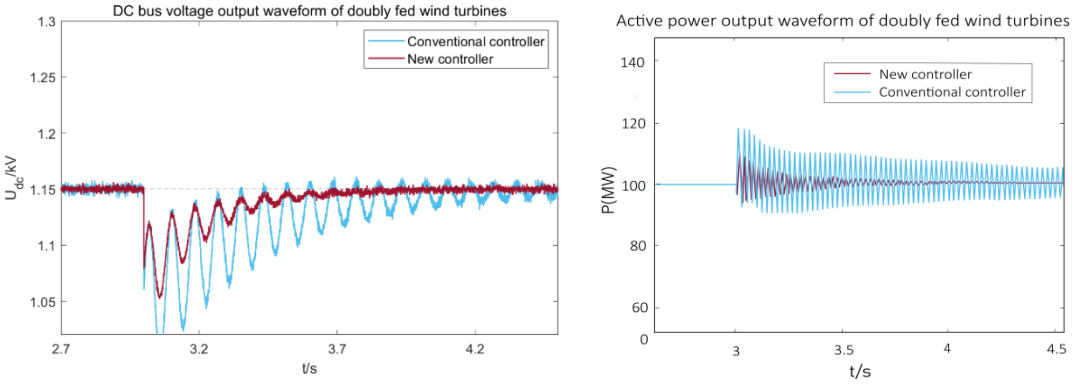

Figure 22 Working Condition B: Bus voltage output waveform of a doubly fed generator

Figure 23 Working Condition B: Active power output waveform of a doubly fed generator

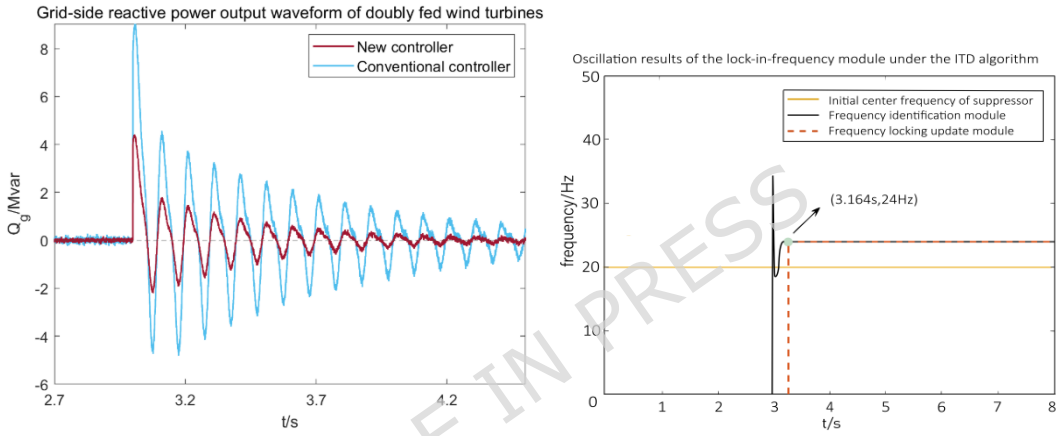

Figure 24 Working Condition B: Qg output waveform of a doubly fed generator

Figure 25 Working Condition B: Small interference oscillation detection results

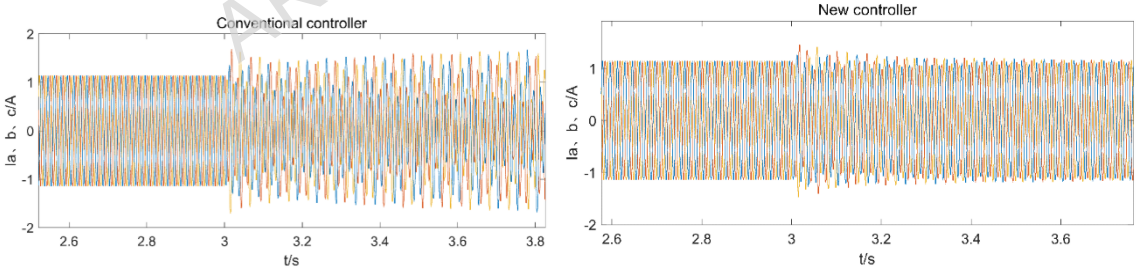

Figure 26 Working Condition C: Three-phase stator current output waveform of doubly-fed fan

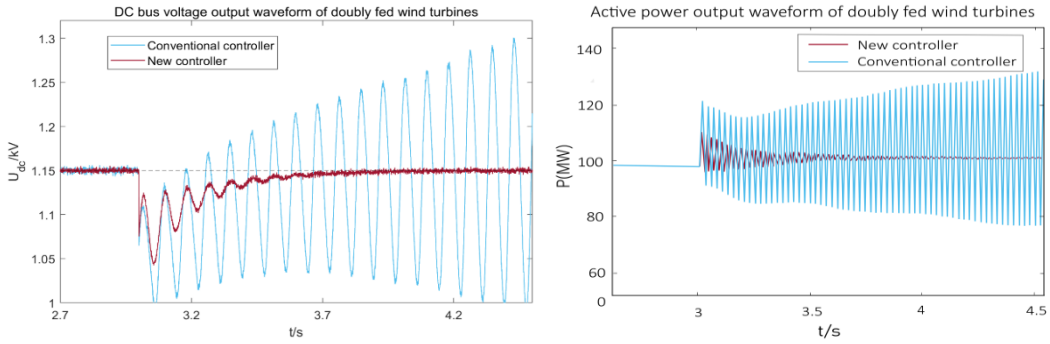

Figure 27 Working Condition C: Bus voltage output waveform of a doubly fed generator

Figure 28 Working Condition C: Active power output waveform of doubly-fed fan

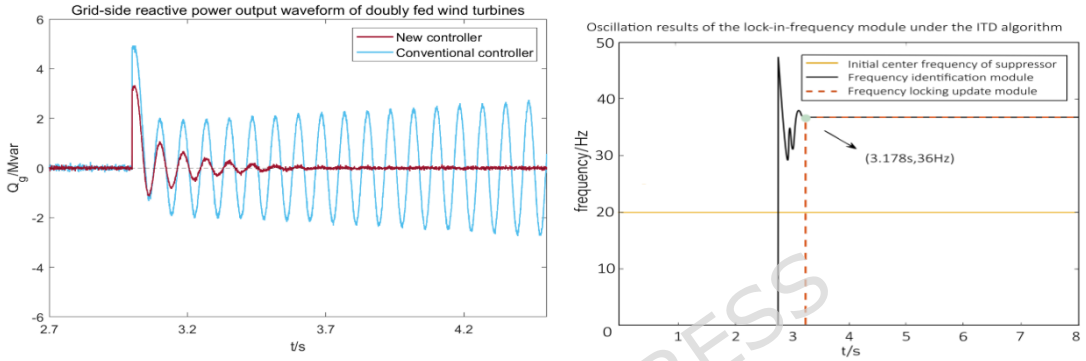

Figure 29 Working Condition C: Qg output waveform of a doubly fed generator

Figure 30 Working Condition C: Small interference oscillation detection results

Table 5. Performance indicators of output power of different suppressors under three operating conditions

Metric	Conventional controller	New controller
A□Overshoot (%)	7.511	6.183
A□Settling time (±2%) (s)	0.457	0.251
A□Steady-state error e_{ss}(MW)	0.176	0.152
A□Total power output(MW)	135.47	137.88
B□Overshoot (%)	18.609	9.802
B□Settling time (±2%) (s)	1.053	0.318
B□Steady-state error e_{ss}(MW)	1.055	0.276
B□Total power output(MW)	147.831	152.712
C□Overshoot (%)	21.503	0.281
C□Settling time (±2%) (s)	1.178	0.283
C□Steady-state error e_{ss}(MW)	3.101	0.347
C□Total power output(MW)	164.821	155.301

6. Conclusions

In order to impede the propagation of small-signal oscillation frequency within the rotor-side converter of a doubly fed wind turbine system connected to the grid via a series-compensated transmission line, while simultaneously considering the impact of real-time variations in small-signal oscillation frequency on system stability, this paper proposes a small-signal oscillation suppression strategy based on the joint control of LADRC and AQPR for doubly fed wind turbines. The main

findings are as follows.

1) For the small-signal oscillation frequencies existing in the current inner loop of the rotor-side converter of a doubly fed wind turbine, replacing the conventional PI controller with a linear active disturbance rejection controller (LADRC) can effectively block the propagation of these oscillations. Experimental results demonstrate that the LADRC controller achieves fast and accurate tracking of the current inner-loop control objectives of the rotor-side converter, and its control performance is significantly superior to that of the traditional PI controller.

2) For the time-varying small-signal oscillation frequencies arising from the cross-coupling effects in the rotor-side converter of a doubly fed wind turbine, an adaptive quasi-proportional resonant (AQPR) suppressor, constructed by combining the intrinsic timescale decomposition (ITD) algorithm with a frequency-locked update module, is proposed. By appropriately tuning the key parameters of the AQPR suppressor, this issue can be effectively addressed. Comparative experimental results with the conventional PR controller indicate that the AQPR suppressor provides more effective suppression of small-signal oscillations over a wide frequency range with real-time frequency variations.

3) Based on a doubly fed wind turbine grid-connected system with series-compensated transmission lines, a comprehensive suppression strategy integrating LADRC and AQPR is developed. By systematically considering the stability issues induced by small-signal oscillations in the system, simulation results verify that the proposed suppression strategy can significantly enhance the disturbance rejection capability of the overall system under small-signal oscillation conditions, thereby ensuring the stable operation of the grid-connected doubly fed wind turbine system.

Author Contributions: Conceptualization, L.C.（Chenchen Li）, L.C.（Chunhui Liang）.; methodology, L.C.（Chenchen Li）, L.C.（Chunhui Liang）; software, L.C（Chenchen Li）., H.C.; validation, L.R., H.C.; formal analysis, Z.S.（ZhangShuyu）; investigation, L.C.（Chenchen Li）, Z.S.（ZhangShuyu）, and L.R.; resources, L.C.（Chunhui Liang）; data curation, L.R., H.C.,Z.J.; writing—original draft preparation, L.C.（Chenchen Li）, and L.C.（Chunhui Liang）; writing—review and editing, Z.S.（ZhangSongcai）; visualization, H.C.; supervision, Z.S.（ZhangSongcai）, and L.R.; project administration, Z.J., L.C.（Chenchen Li）; funding acquisition, L.C.（Chunhui Liang） All authors have read and agreed to the published version of the manuscript.

Funding: This research was funded by Jilin Provincial Department of Science and Technology (20230402062GH).

Institutional Review Board Statement: Not applicable.

Informed Consent Statement: Not applicable.

Data Availability Statement: Data is provided within the manuscript or supplementary information files.

Acknowledgments: The authors would like to thank the university for providing a conducive atmosphere to conduct this research.

Conflicts of Interest: The authors declare no conflict of interest.

Reference

1. Liu, F., Sun, F., Wang, X.: Impact of turbine technology on wind energy potential and CO2 emission reduction under different wind resource conditions in China. Applied Energy. 348:121540(2023). https://doi.org/10.1016/j.apenergy.2023.121540

2. Shair, J., Xie, X., Wang, L., Liu, W., He, J., Liu, H.: Overview of emerging subsynchronous oscillations in practical wind power systems. Renewable and Sustainable Energy Reviews. 99: 159-168(2019). https://doi.org/10.1016/j.rser.2018.09.047
3. Rua, P., Roose, T., Sakinci, O., Shao, H., Beerten, J.: Identification of mechanisms behind converter-related issues in power systems based on an overview of real-life events. Renewable and Sustainable Energy Reviews. 183: 113431(2023). https://doi.org/10.1016/j.rser.2023.113431
4. Xie, MT., Zhang, X., Liu, H.: Characteristic analysis of sub-synchronous resonance in practical wind farms connected to series-compensated transmissions.IEEE Transactions on Energy Conversion. 32:1117-1126(2020).
5. Bodapatla S K, Gaddam M, Sarma P M. Robust H-infinity and μ-synthesis controllers to mitigate sub-synchronous control interaction in DFIG wind farms considering time delay[J]. Electrical Engineering, 2024, 106(5): 6019-6034.
6. Feng X, Wen T, Liu X, et al. Mitigating SSR of series-compensated DFIG wind farms based on cascaded high-gain state and perturbation observers[J]. CSEE Journal of Power and Energy Systems, 2025.
7. Liu Q, Wu J, Wang H, et al. Analysis of DFIG interval oscillation based on second-order sliding film damping control[J]. Energies, 2023, 16(7): 3091.
8. Xiang S, Su P, Wu X, et al. Comparative Study and Optimal Design of Subsynchronous Damping Controller in Doubly Fed Induction Generator[J]. Sustainability, 2022, 14(20): 13095.
9. Li, P., Wang, Jie., Xiong, L., Ma, M.,Wang, Z., Huang,S.: Mitigating subsynchronous control interaction using fractional sliding mode control of wind farm. Journal of the Franklin Institute. 357: 9523-9542(2020). https://doi.org/10.1016/j.jfranklin.2020.07.024
10. Xue T, Karaagac U, Ghafouri M, et al. Review on DFIG Supplementary SSI Damping Controllers: Design, Development, and Directions[J]. IEEE Transactions on Power Delivery, 2025.
11. Xiang S, Su P, Wu X, et al. Comparative Study and Optimal Design of Subsynchronous Damping Controller in Doubly Fed Induction Generator[J]. Sustainability, 2022, 14(20): 13095.
12. Han, R., Hu, Q., Fang, X., Qian, T., Zhang,Y.: Frequency security-constrained unit commitment with fast frequency support of DFIG-based wind power plants. International Journal of Electrical Power & Energy Systems.160:110119(2024).https://doi.org/10.1016/j.ijepes.2024.110119
13. Shair, J., Xie, X., Li, Y.: Hardware-in-the-loop and field validation of a rotor-side subsynchronous damping controller for a series compensated DFIG system. IEEE Transactions on Power Delivery.36:698-709(2021).https://ieeexplore.ieee.org/document/9076312
14. Moradi, Z.: Proposed sub-synchronous resonance damping controller for large-scale wind farms.IET renewable power generation. 13: 3209-

3220(2023). https://www.zhangqiaokeyan.com/journal-foreign-detail/0704082809425.html

15. Chao W , Deng C , Huang J ,et al.A Sub-Synchronous Oscillation Suppression Strategy Based on Active Disturbance Rejection Control for Renewable Energy Integration System via MMC-HVDC[J].Electronics, 2023, 12(13):21.DOI:10.3390/electronics12132885.
16. Zheng J , Li B , Zhang Y L Y C Q .HPF-LADRC for DFIG-based wind farm to mitigate subsynchronous control interaction[J].Electric Power Systems Research, 2023, 214(Jan. Pt.B):1-10.DOI:10.1016/j.epsr.2022.108925.
17. Yu, SS.: An Optimized Power-Angle and Excitation Dual Loop Virtual Power System Stabilizer for Enhanced MMC-VSG Control and Low-Frequency Oscillation Suppression. Energies. 17: 4711(2024). http://www.mdpi.com/1996-1073/17/18/4711/html
18. Chen Y , Wu F , Shi L ,et al.Analysis and Suppression Strategies of Sub-Synchronous Oscillations in DFIG Wind Farm Integrated with Synchronous Pumped Storage System[J].Sustainability (2071-1050), 2025, 17(10).DOI:10.3390/su17104588.
19. Broens, Y.,Butler, H.: Frequency Domain Auto-tuning of Structured LPV Controllers for High-Precision Motion Control. Electrical Engineering and Systems Science. 16:10-16(2024).https://arxiv.org/abs/2403.05878?context=cs
20. Xue T , Karaagac U , Ghafouri M ,et al.Review on DFIG Supplementary SSI Damping Controllers: Design, Development, and Directions[J].IEEE Transactions on Power Delivery, 2025(2):40.DOI:10.1109/TPWRD.2025.3525551.
21. Gong, Y., Huang, Q., Cai, D., Olorunfemi, B.:Characteristics of sub-synchronous oscillation in grid-connected wind farm system. Journal of Electronic Science and Technology. 21: 100228(2023). https://doi.org/10.1016/j.jnlest.2023.100228
22. Guo, H., Wang, C., Yang, L., Xia, M., Liu, Z., Zhang, X.: Subsynchronous oscillation suppression strategy of wind turbine's phase-locked loop based on optimal damping ratio. Energy Reports. 11: 3088-3095(2024). https://doi.org/10.1016/j.egyr.2024.02.009
23. Shair, J., Xie, X., Yan, G.: Mitigating subsynchronous control interaction in wind power systems: Existing techniques and open challenges. Renewable and Sustainable Energy Reviews. 108: 330-346(2019). https://doi.org/10.1016/j.rser.2019.04.003
24. Chen, X., Liu, Z.: Impedance Modeling and Stability Analysis of the Converters in a Double-Fed Induction Generator (DFIG)-Based System. Energies. 12: 1-23(2019).https://EconPapers.repec.org/RePEc:gam:jeners:v:12:y:2019:i:13:p:2500-:d:243857
25. Yuan, D., Ma, X., Zeng, Q.: Research on frequency-band characteristics and parameters configuration of linear active disturbance rejection control for second-order systems. Control Theory Applications. 30: 1630-1640(2016).

26. Meng, F., Sun, D., Zhou, K.: A subsynchronous oscillation suppression strategy for doubly fed wind power generation system. IEEE Access. 9: 83482-83498(2021).
27. Khomsi, C., Bouzid M., Jelassi, K.: Harmonic current conpensation in a single-phase grid connected photovoltaic system sypplying nonlinear load. International Renewable Energy Congress. 331: 120270(2018). https://doi.org/10.1109/IREC.2018.8362520
28. Zammit, D., Cyril, S., Apap, M., Licari, J.: Design of PR current control with selective harmonic compensators using Matlab. Journal of Electrical Systems and Information Technology. 4: 347-358(2017). https://doi.org/10.1016/j.jesit.2017.01.003
29. Chen, D,. Guo, Z,. Chen, X.: Quasi-PR multi-layer photovoltaic grid-connected control based on frequency feedback. 2022 IEEE International Conference on Electrical Engineering, Big Data and Algorithms (EEBDA).2022.810-814.
30. Ledesma P , Usaola J .Doubly fed induction generator model for transient stability analysis[J].IEEE Transactions on Energy Conversion, 2005, 20(2):388-397.